JOURNAL OF SPACECRAFT AND ROCKETS
Vol. 35, No. 4, July–August 1998

Aerothermodynamics of a Parashield Re-Entry Vehicle

Harry K. Magazu,* Mark J. Lewis,† and David L. Akin‡
University of Maryland, College Park, Maryland 20742-3015

Feasibility and performance are investigated for a baseline configuration of a parashield re-entry vehicle, so named because it combines features of a parasol in a folding heatshield that might also be used as a landing parachute. The flowfield properties and heat transfer response are calculated for a 150-kg, 2.6-m-diam baseline parashield vehicle on a re-entry trajectory from low Earth orbit. The re-entry shield is formed from high-temperature cloth stretched over rigid folding spars and has a very low ballistic coefficient. Calculations show that a parashield made of 3M-brand Nextel™ 312 AF-10 ceramic fabric deployed over 12 Al 2024 arced spars designed for 15-deg angle of attack could withstand the re-entry aerothermodynamic stagnation-point heating load from a 122-km circular orbit. During this re-entry, the vehicle would experience a maximum 3.4 *g* of deceleration and would have a payload mass fraction of up to 45% with great packaging flexibility. Panel and spar heating, shield permeability, angle-of-attack misprediction, and free shear layer impingement are shown to be manageable design issues for a flexible cloth shield. It is also shown that the baseline vehicle could be scaled upward in size by at least a factor of 10 for increased payload volume and mass.

Nomenclature

A_s	= main shield area, m^2
a	= panel length, m
C_d	= drag coefficient, $D/(q_\infty S)$
d	= fiber diameter, m
E	= modulus of elasticity, GPa
k	= permeability constant, m^2
L/D	= lift/drag
M	= Mach number
p	= pressure, N/m^2
q	= stagnation-point aerodynamic heating rate, W/m^2-s
R_c	= radius of curvature, m
Re	= Reynolds number
T	= temperature, K
t	= thickness, m
V	= velocity, m/s
w	= surface deflection, m
X_s/R_s	= shield bluntness parameter
x	= panel surface coordinate in radial direction, m
y	= panel surface coordinate in azimuthal direction, m
α	= angle of attack, deg
β	= ballistic coefficient
δ	= shock-layer thickness, m
η	= shield surface angle relative to axis of symmetry, deg
θ	= radial angle relative to axis of symmetry, deg
θ_s	= maximum subtended shield angle, deg
μ	= dynamic viscosity, m^2/s
ν	= Poisson ratio
ϕ	= fabric to spar tangency angle and free shear layer impingement angle, deg
ψ	= shield azimuthal angle, deg

Subscripts

filter	= property of the internal flow through the main shield
n spars	= value of a vehicle with n spars supporting the main shield
stag	= main shield stagnation-point value
0	= total or reference value
312	= Nextel™ 312, AF-10 property
∞	= freestream flow properties

Received July 15, 1997; revision received Dec. 15, 1997; accepted for publication April 8, 1998.

*Graduate Research Assistant, Department of Aerospace Engineering. Student Member AIAA.

†Associate Professor, Department of Aerospace Engineering. Associate Fellow AIAA.

‡Associate Professor, Department of Aerospace Engineering. Senior Member AIAA.

Introduction

THE parashield is a flexible, semiballistic, re-entry, aerobrake or aeroassist vehicle, which has a very low ballistic coefficient. This is accomplished by deploying a large-area woven ceramic fiber-based thermal blanket over folding, circularly arced radial spars, in a manner resembling an ordinary umbrella. The advantage of this concept for re-entry design is that a large shield can be packaged in a small volume for launch or on-orbit storage without the structural limitations and impact vulnerability of an inflatable structure. The feasibility of constructing such a shield is suggested by the availability of high-temperature ceramic cloths, such as 3M brand Nextel™ 312. This work will show that the large radius of curvature made possible with a deploying flexible shield results in heating rates that can in turn be handled by such materials. As is also shown, the use of a flexible re-entry shield made from porous cloth supported on spars has associated with it several unique structural and aerodynamic issues, primarily related to departures from true spherical geometry, surface flow penetration, and surface deflections.[1]

A parashield design could satisfy the need for enhanced flexibility in the re-entry of general scientific and commercial payloads from Earth orbit to build and expand a permanent commercial and scientific space presence; the potential demand for ready return of experiments and cargo from the International Space Station; and the manned interplanetary, lunar return, and deep-space missions made possible by an aeroassisted space transfer vehicle. For instance, one use for small parashields would be the individual re-entry of scientific and commercial payloads from satellites and vehicles remaining in orbit, such as a routine space station data drop. These small parashield designs could be scaled up and deployed by the Space Shuttle or a single-stage-to-orbit rocket for lunar return and aeroassisted satellite transfer missions, and could be used as part of the assured crew re-entry vehicle. A personal parashield might be an attractive option for individual or multiperson-crew escape from the station. Through the permanent on-orbit support of the space station and/or the launch mass capability of the Shuttle or a single-stage vehicle, the parashield even holds promise for viable launch and deployment on the scale required for crewed interplanetary and deep-space aeroassist missions.

Recent aeroassist and ultralow ballistic coefficient vehicle research has supported the baseline analysis of the lunar return and crewed Mars missions outlined by the space exploration initiative and the development of NASA's now canceled Aeroassist Flight Experiment (AFE). This present effort relies on the Earth entry corridor

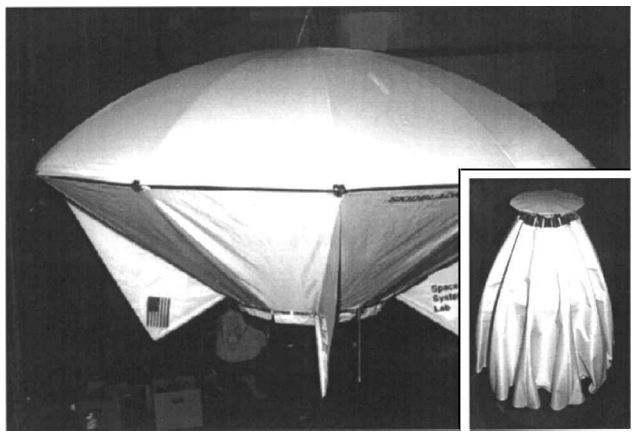

Fig. 1 Photograph of deployed parashield re-entry vehicle; inset shows the vehicle stowed.

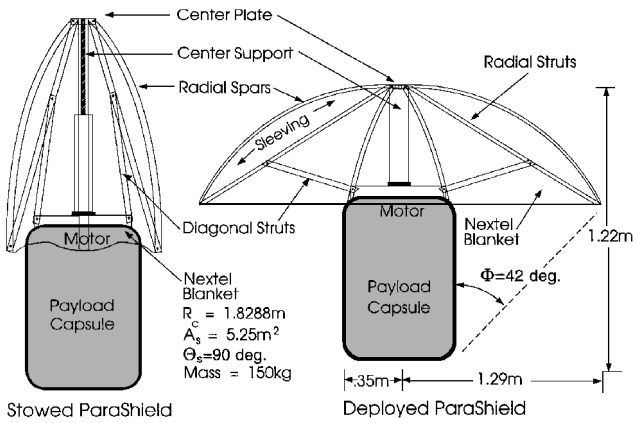

Fig. 2 Parashield re-entry vehicle baseline geometric specifications.

and trajectory analysis by Braun and Powell[2]; sizing and structural modeling by Raju and Craft[3]; stagnation-point heating and thermal-protection system analysis by Tauber et al.[4]; angle-of-attack misprediction studies by Freeman et al.[5]; and wake packaging, shear-layer isolation, and payload heating by Gnoffo et al.[6] and Strawa et al.[7]

This study has attempted to provide an integrated treatment of the aerothermodynamic and materials issues associated with a specific flexible ultralow ballistic coefficient vehicle design, originally proposed and constructed for a parashield suborbital flight test experiment shown in Fig. 1. This parashield was intended for launch on a hybrid-propellant booster, but a launch failure prevented successful deployment (though the parashield did in fact survive this event).[8] To fit the original booster payload volume, it has a 2.58-m-diam shield with a 1.8-m radius of curvature that folds to a 0.8-m-diam package for launch or storage, with a corresponding frontal area that varies by a factor of 10 from a folded 0.50 m^2 to a deployed 5.25 m^2. This geometry, shown in Fig. 2, has a 1.22-m-long, 0.7-m-diam cylindrical payload region. The geometric specifications for this existing hardware are used as a baseline configuration; variations in the number of radial spars, spar cross-sectional shape, and main shield thickness are studied parametrically. The continuum low-Earth-orbit (LEO) re-entry aerothermodynamic stagnation-point environment and induced vehicle response are outlined, accounting for angle-of-attack misprediction and materials issues. Another problem of unique interest for a re-entering parashield, that each spar may have associated with it a local stagnation region, is also discussed, though the possibility that flexing material may generate unsteady flows in the shield wake is neglected in this analysis.

Parashield Aerodynamic Analysis

Aerodynamic Coefficients

The 150-kg baseline parashield geometry, shown in Fig. 1, uses 12 radial spars to generate a nearly spherical shock layer, maintains a ballistic coefficient of $\beta = 181$ Pa, and generates a continuum hypersonic L/D of 0.18 at an angle of attack of 15 deg. The continuum hypersonic lift and drag coefficients were first estimated using modified Newtonian impact theory:

$$Cp_{\text{local}} = Cp_{\max}(\sin\eta\cos\alpha - \cos\eta\cos\psi\sin\alpha)^2 \tag{1}$$

$$Cp_{\max} = \frac{2}{\gamma M_\infty^2}\left\{\left[\frac{(\gamma+1)^2 M_\infty^2}{4\gamma M_\infty^2 - 2(\gamma-1)}\right]^{\gamma/(\gamma-1)} \times \left(\frac{1-\gamma+2\gamma M_\infty^2}{\gamma+1}\right) - 1\right\} \tag{2}$$

Equation (1) was integrated over the main shield surface and was normalized by the vehicle base area to obtain the normal and axial aerodynamic force coefficients

$$C_n = \frac{2}{A_s}\int_{\theta=0}^{\theta=\theta_s/2}\int_{\psi=0}^{\psi=\pi} -Cp_{\max}\sin^2\theta\cos\psi R_c^2\,\mathrm{d}\psi\,\mathrm{d}\theta \tag{3}$$

$$C_a = \frac{2}{A_s}\int_{\theta=0}^{\theta=\theta_s/2}\int_{\psi=0}^{\psi=\pi} +Cp_{\max}\sin\theta\cos\theta R_c^2\,\mathrm{d}\psi\,\mathrm{d}\theta \tag{4}$$

which were then used to calculate lift and drag

$$\frac{L}{D} = \frac{C_n\cos\alpha - C_a\sin\alpha}{C_a\cos\alpha + C_n\sin\alpha} \tag{5}$$

The variation in aerodynamic coefficients with angle of attack α was calculated for a parametric range of parashields supported by various numbers of odd and even radial spars in addition to the baseline design. Each geometry was chosen with an identical base area and shield bluntness to isolate the effect of the variation in the number of radial spars on the L/D and required trim α of both symmetrical and horizontally asymmetrical parashields with equal ballistic coefficients.

The results of the spar study are shown in Fig. 3. Note that even-paneled geometries produce identical normal and axial coefficients due to their symmetry, and odd-paneled vehicles generate a variable normal coefficient due to their horizontal asymmetry. Therefore, odd-paneled vehicles generate greater lift and nearly constant drag when compared to the even-paneled configurations at a constant α. The magnitude of this effect decreases as the number of shield panels is increased and the shield becomes more nearly spherical. The minimum number of spars for shield support is three; for α less than 25 deg, the maximum difference in the L/D of a 12-paneled and a 3-paneled parashield is 5.5%. Thus, the maximum decrease that could be achieved in the trim α of the baseline parashield is 2 deg if the number of radial spars were decreased from 12 to 3. This decrease in trim α would increase the protected shadow region for payload packaging region, but would likely reduce stability and increase panel concavity along with increasing surface fluttering and aerodynamic heating at the shield-to-spar interfaces.

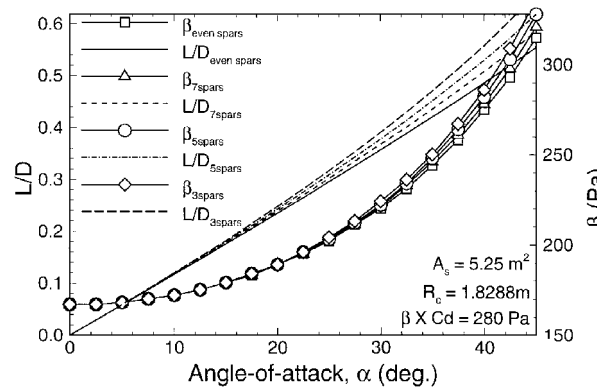

Fig. 3 Parashield L/D and ballistic coefficient β vs main shield panels.

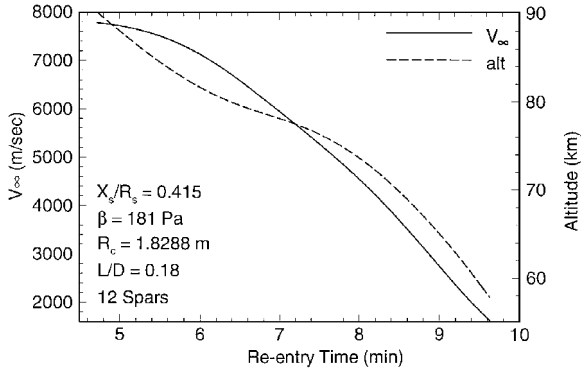

Fig. 4 Parashield LEO re-entry altitude and velocity histories.

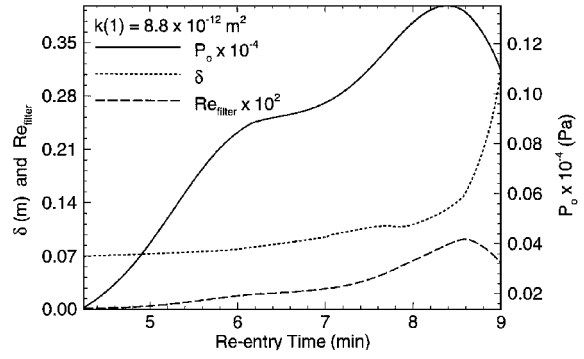

Fig. 5 Parashield LEO re-entry total pressure, shock detachment distance, δ, and filter Reynolds number histories.

Baseline Re-Entry Trajectory

Calculations of the parashield's aerothermodynamic properties, including equilibrium chemistry, were performed using published correlations[9] nested within a fourth-order Runge–Kutta numerical integration of the standard trajectory equations.[10] Calculations were performed in the U.S. Standard Atmosphere[11] starting at the parashield's re-entry interface at 7.8 km/s, 0.614-deg flight-path angle, and 122-km altitude. The calculations of the parashield's trajectory, inviscid shock-layer properties, and flowfield chemical composition were advanced by $\frac{1}{2}$-s intervals beginning at 92-km altitude and Knudsen number = 0.013 (based on shield diameter) to provide a complete profile of stagnation-point heating rates along the trajectory.

As shown in Fig. 4, the parashield enters the continuum flow regime 5 min after deboost; within $4\frac{1}{2}$ min the parashield decelerates to 1.6 km/s and has descended to 57.5-km altitude. The peak deceleration experienced is 3.4 g, at 3 km/s and an altitude of 66 km. The shock-layer temperature is initially 5400 K and peaks at 5500 K before rapidly decreasing. The parashield's aerodynamic pressure loading is initially 200 Pa but rapidly increases with the vehicle's deceleration, peaking at 8.4 min, slightly before maximum deceleration. The maximum total pressure is 1350 Pa and occurs at 4 km/s, Mach 13, and 68-km altitude. The region of peak aerodynamic loading, which occurs between 8 and 9 min, is the critical time period for structural analysis and was, therefore, chosen for detailed numerical validation.

In addition to the on-design conditions, the sensitivity of the magnitude and altitude of the maximum deceleration and total pressure loading to variations in trim angle of attack α was also investigated. Within a misprediction range of ± 5 deg in α, the magnitudes of the peak aerodynamic characteristics outlined did not vary by more than a few percent.

Aerodynamic Effects on Woven Fabric Permeability

A fundamental issue in the aerodynamic analysis of the parashield is the applicability of the solid wall boundary condition when the pressure bearing surface is a permeable taut fabric. If a substantial volume of the parashield's shock layer passes through the thermal-protection system, high-energy chemically reacting flow will impinge directly on the payload, obviously defeating the fundamental purpose of the thermal-protection system. Similarly, if considerable mass penetrates and decelerates within the cloth wall, molecular recombination within the thermal blanket matrix may pull the bow shock closer to the vehicle than is expected. Thus, with significant mass entrainment and flow seepage at the wall, the earlier determined aerodynamic coefficients, trajectory calculations, and shock-layer properties will be inaccurate. Even worse, seepage could create destructive heating inside the cloth and magnify the temperature gradients at the wall. Therefore, the minimization of shock-layer flow seepage and shield penetration are critical parashield design issues.

The parashield material is modeled as a filter, with a measured permeability to characterize the volumetric flow per area that passes through the porous medium at a given pressure difference.[12] It is assumed that such is governed by Darcy's law of filtration

$$\nabla p \propto \nabla^2 V \tag{6}$$

for internal filter flows meeting local Stokes flow assumptions. For one-dimensional filter flow, this reduces to

$$v_{\text{seep}} = \frac{k_{312}\Delta p_0}{\mu_{\text{air}} t_{\text{shield}}} \tag{7}$$

$$Re_{\text{filter}} = \frac{\rho_2 v_2 d_{312}}{\mu_2} \tag{8}$$

which relates the seepage velocity to the filter thickness, the total pressure difference, the filtered media viscosity, and the filter material internal geometry, through the permeability constant k. The experimentally determined Nextel 312 permeability constant for a single layer of AF-10, five-harness, satin weave cloth at an industrial-standard pressure difference of 125 Pa (Ref. 13) is 8.8×10^{-12} m^2 (Ref. 14). In comparison, AF-40 fabric is a five-harness satin weave of precisely four times the thickness of AF-10 with measured seepage velocity of 0.1015-m at 125 Pa (Ref. 14). This equates to a linear 25% decrease in volumetric seepage per unit area, per additional layer of Nextel AF-10, and allows for the calculation of the Darcian permeability constant of the parashield main shield as a linear function of thickness.

Figure 5 shows the histories of the total pressure loading of the parashield main shield, the shock-layer thickness, and the internal (or filter) Reynolds number expressed by Eq. (8). The internal Reynolds number is referenced to the Nextel fiber diameter and the stagnation-point boundary-layer edge velocity. Note that, because the characteristic dimension and local flow velocity are small, the filter Reynolds number is much smaller than unity[12,15] and the capture particle-to-filter fiber diameter ratio for diatomic air molecules and Nextel 312 fibers is on the order of 10^{-5}. This last condition indicates that particle capture will involve primarily one fiber and verifies the applicability of single-fiber filter theory.[12,15] These two conditions justify the modeling of the shield seepage as a local Stokes flow and confirm its governance by a linear relationship between wall thickness and capture efficiency, i.e., capture cross section per unit area, and Darcy's law relating the seepage velocity to the total pressure difference.[12,15]

The Nextel 312 geometric filter constant was calculated for the baseline parashield assuming a linearly increasing capture efficiency with increased thickness. Darcy's law was then used to determined the seepage velocity vs the total pressure difference at each point along the trajectory, using curve-fit approximations referenced to the freestream static temperature to calculate the viscosity of air vs temperature.[16] Temperature inside the wall was always less than the material failure temperature of 1200 K, so real gas effects on transport properties were not significant. The maximum volume seepage per unit area, as a percentage of the shock-layer thickness at the stagnation point, was then calculated as a function of the parashield shield thickness over the outlined trajectory. After detailed studies, a flow seepage of 1% of the shock-layer volume was somewhat arbitrarily chosen as a reasonable maximum tolerable seepage for application of the solid wall boundary condition. This was found to require 26 layers of AF-10. Each layer is 0.25 mm thick; therefore, the parashield fabric shield must be 6.5 mm thick and will have a mass of 34.5 kg. Sensitivity studies showed that a 5.5-mm-thick

shield with mass of 29.2 kg would have 2.6% seepage, whereas a 7.5-mm, 39.8-kg shield thickness would have about 0.25% seepage. Thus, an extra 5.3 kg reduces seepage by a factor of 4, which, depending on thermal constraints for the payload behind the shield, might be a desirable trade. Note that additional fabric might be required to protect each support spar, depending on the choice of spar material, as will be described next.

Aerodynamically Induced Main Shield Deformation

It was found that the parashield fabric shield would experience a 1350-Pa pressure loading if it were to behave as a solid wall; in reality, the flexible fabric shield will actually tend to become concave between the parashield load-bearing spar structures, creating considerable shear within the panels and possibly complex flow patterns. This potential shield concavity was modeled to provide conservative engineering estimates of the likely amount of deformation and the maximum pretension required to resist it.

The deformation of an equilateral triangle-shaped uniformly stretched and uniformly loaded impermeable membrane, clamped on two sides, is the same as the bending of an equilateral triangular plate by uniform moments resolved at two clamped edges.[17] The three-dimensional relation of surface deflection of such a plate is

$$w_{312} = \frac{3p\left(1-\nu_{312}^2\right)}{16aE_{312}t_{\text{shield}}^3}\left[x^3 - 3y^2x - a(x^2+y^2) + \frac{4a^3}{27}\right] \times \left[\frac{4a^2}{9} - x^2 - y^2\right] \tag{9}$$

The full derivation and analogy of these relations to the problem at hand has been presented by Timoshenko and Woinowsky-Kreiger.[17]

Centerline deflection of the 12-paneled parashield's edge was predicted for the case of a 1350-Pa uniform pressure load. The modulus of elasticity for Nextel 312 is 138 GPa (Ref. 14). Based on the work of Fogal,[13] Poisson's ratio was estimated to be 0.20 for Nextel 312 AF-10, which is the experimentally determined value for most open weave fabrics of this type. With the Nextel AF-10 modulus of elasticity and the earlier calculated parashield main shield fabric thickness of 6.5 mm, the maximum edge deflection of the 12-paneled parashield was found to be 1.8 cm, which corresponds to a 1% centerline deflection referenced to panel width in the normal direction.

To calculate the maximum deployable pretension within the parashield main shield, it was assumed that the fabric deflection would form a catenary (a two-dimensional approximation to the fully three-dimensional deformation), which was fitted between the spars. This catenary function with determined maximum deflection was numerically integrated to calculate the induced pressure and panel edge elongation. The maximum deployable pretension was then calculated from a linear relationship derived for the aerodynamically induced fabric tension as a function of the ratio of the induced Nextel 312 AF-10 deformation length to the material's elongation tolerance and its tensile strength, 1725 MPa. Assuming a safety factor of 1.5 (Refs. 1 and 14), it was found that 1500 MPa would be sufficient shield pretension to maintain fabric tautness and to resist edge flutter along the specific chosen re-entry trajectory.

Nextel 312 fibers can be elongated by only 1.012 times their original length before they fail.[14] A catenary was fitted between spars with a numerically integrated edge dimension set equal to this maximum deformation length, from which the maximum tolerable centerline edge deflection in the normal direction was found to be 4.54 cm for the 12-paneled parashield. This concavity limit corresponds to a 7% centerline deflection by panel width. Furthermore, by measuring the tangent of the catenary deformation pattern at the pinned supports, the maximum expected fabric-to-spar attachment angle during the chosen re-entry trajectory would be 15 deg. Despite the modest value of this worst-case tangency angle between the fabric panels and the spar bond interfaces, a more detailed analysis of the effect of shield deformations (due to spar protrusion) on the aerothermodynamic performance would be desirable to confirm parashield flight worthiness.

Because the parashield is formed from stretched panels, its flowfield may have some differences from that of a perfect sphere. An indication of this is seen in Fig. 6, which is a contour plot of inviscid-flow static pressure contours on a flat-paneled parashield (left-hand side) and a parashield with maximum cancavity before material failure (right-hand side). Properties were calculated for the inviscid flowfield using Walter's GASP code on a three-dimensional three-zone O grid generated with GridGen version 8 (Refs. 18 and 19). The computational scheme is three-dimensional, finite volume, second-order-accurate upwind, with spatial discretization of variables, solved through an implicit three-factor approximate factorization method, using Van Leer's flux-vector splitting algorithm. MUSCL was used for extrapolation in the discretization of the spatial variables. The aft region was not included in the calculation.

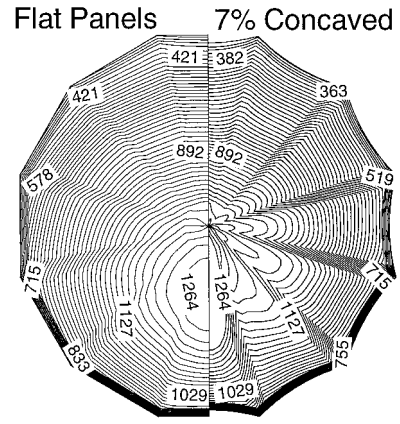

Fig. 6 Parashield inviscid computational static pressure contours on the main shield surface for 12 panels: α = 15 deg, M_∞ = 13, and P_∞ = 28 Pa.

Note that each protruding spar in Fig. 6 will create a stagnation-line region with increased pressure, with an expected increase in heating rate. Even the flat-paneled parashield, with no aerodynamic-induced deformation, shows elevated pressures at the spar location. These effects will be considered in the heat transfer analysis. Note also that concavity at the edges of the shield will form a corresponding vortical structure in the base region.

Geometric Scaling

The thermal-protection system weight-to-area ratio is approximately constant, and so the overall heat shield weight scales with base area instead of with vehicle volume, as is the case with traditional phenolic ablators and/or radiative tiles.[4] This scaling rule suggests that a larger parashield would have greater payload mass and volumetric advantages than similarly scaled up semiballistic or lifting systems. Note that the area over which pressure forces would act to deform the parashield and, therefore, total deforming force will scale with the vehicle, so that there is greater potential for unacceptably deep concavity of the parashield panels as the geometry is scaled up.

To study scaling effects, the triangular membrane and catenary-fit deformation analysis was also performed for 12-paneled parashields with 5, 10, and 20 times the length dimensions of the baseline vehicle. The 5- and 10-fold scaled up parashields would have a worst-case 2.4% and 3.7% concavity by width, respectively, whereas even a shield 20 times larger than the baseline geometry experienced 6.8% panel concavity by width, at the limits of material properties.

Spar Deformation

Referring back to Fig. 2, the baseline parashield's deployment mechanism was designed to help minimize beam bending and to reduce the probability of edge oscillations. This further helps assuage the outlined concerns of aeroelastic instability, flutter, and vibrationally induced flow separation. Through the use of radial struts with pinned supports, the maximum spar deflection point is moved from the edge to the spar center. The radial struts are tension-bearing members, which help to counter the radial spar's normal deformation by resisting edge separation. Further, a portion of the normal bending force translates through the system into the diagonal struts.

The radial spar's maximum deflection, internal shearing force, and bending moments were estimated assuming that the maximum aerodynamically induced total pressure, 1350 Pa, is a one-dimensional uniform loading acting on the deflection of a simply supported beam.[20] This simplified model neglects the beneficial effects of the deployed truss geometry. A loading analysis was performed for radial spars consisting entirely of the following commonly available materials: aluminum 2024, beryllium, carbon-carbon composite, copper, stainless steel, and titanium. It was found that each of these materials could withstand the total pressure loading with minimal deflection, ranging from 2 mm for copper to 7 mm for beryllium. Further, the parashield radial spars will be loaded with a maximum shearing force of 92 MPa and a bending moment at the spar center of 112.6 Nm, three orders of magnitude below the maximum allowable loading for each material.[20] Therefore, the selection of the proper spar material can be based solely on the thermodynamic loads and the associated impact on the vehicle's mass budget and cost.

Wake Flowfield Considerations

The design of an ultralow ballistic coefficient re-entry vehicle requires the minimization of the vehicle's weight-to-base area ratio. Therefore, the main shield thickness should be reduced as much as possible, the base area should be maximized, and no aft shield should be used unless necessary. The payload may, however, be endangered without the presence of an aft shield. Experimental, computational, and flight-testing data have all shown that the aft flowfield of such vehicles can create a far more intense payload heating environment than was once expected.[6,7,21] At a minimum, therefore, the payload must be carefully placed within the shield volume. The situation is further complicated if the vehicle uses location of the payload mass as the primary mechanism of c.g. offset. In its entirety, a balance must be made between payload volume, mass placement, and L/D to create a sufficiently protected wake payload packaging region for a parashield re-entry vehicle.

General trends have been described, and prediction mechanisms have been developed, to identify properties of the wake-flow region.[6,21] The primary sources of wake-flow aft body heating are radiation from the wake neck, convection from the recirculating viscous flow, and/or free shear layer's impingement. Because of its low ballistic coefficient, the parashield has been found to generate an essentially nonradiating equilibrium flow shock layer with maximum static temperature below 5500 K. Therefore, the reradiation of aft flow at the wake neck, as experienced by Galileo (with its 45-deg aft cone)[22] and as predicted for the never-flown AFE,[23] is not a driving factor for the parashield.

The primary concern for the aft flow of the parashield is, therefore, the prediction of the angle of the shear layer relative to the vehicle base, so that impingement can be avoided. Shieh and Gay[24] have shown that the shear layer can, under certain conditions, separate and impinge on the aft body, creating local heating rates of the same order of magnitude as those at the stagnation point. Further, Dogra[25] reported that the separation angle appears to be independent of the shield shoulder radius, significantly decreased by increased Knudsen number, and linearly decreased by increased angle of attack.[6] Gnoffo et al.[6] demonstrated this linearity with viscous, chemically reacting computational results for the wind-side shear-layer deflection angle vs α, for M_∞ between 10 and 15 at 65 km.

Extrapolating the linear trends of these data, the angle between the parashield shear layer and vehicle base has been predicted for on- and off-trim angle-of-attack re-entry performance. Figure 7 shows that the 42-deg aft wake packaging region selected for the baseline vehicle geometry, encompasses sufficient conical volume to hold a 1.2-m-long, 0.7-m-diam cylindrical payload within the predicted viscous recirculation region, over the entire range of ±5-deg trim α misprediction. Therefore, free shear-layer impingement on the payload element is not expected to occur during parashield re-entry. Further, the maximum parashield aft body convective heating is predicted to be no greater than 20% of the main shield stagnation-point value, based on the results of Shieh and Gay.[24] For a conventional re-entry shield, this value could be very large, but for the reduced heating rates of a parashield, this should be of less concern.

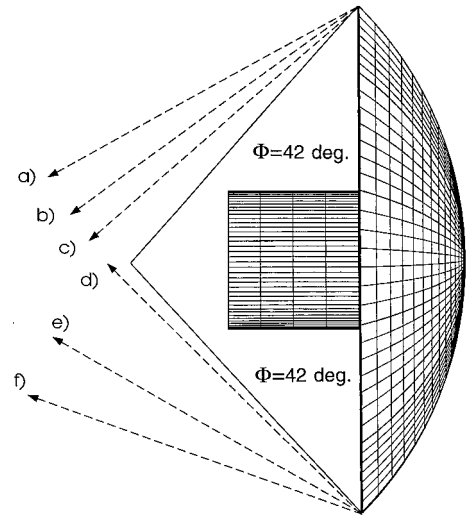

Fig. 7 Parashield LEO re-entry extrapolated aft free shear-layer impingement angle vs angle of attack, from Refs. 6 and 7. Experimental data (deg), Strawa et al.[7]: a) α = 10, Φ = 62; b) α = 15, Φ = 55; and c) α = 20, Φ = 50. Computional data (deg), Gnoffo et al.[6]: d) α = 10, Φ = 70; e) α = 15, Φ = 60; and f) α = 20, Φ = 45.

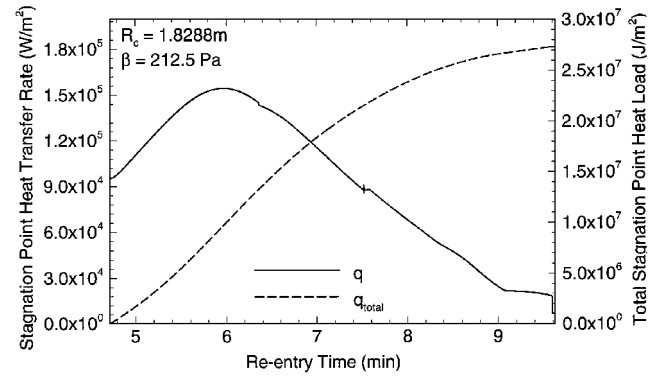

Fig. 8 Parashield LEO re-entry heat transfer rate and total heat load histories.

Parashield Thermodynamic Analysis

Thermodynamic Loading

The classic Fay and Riddell[26] stagnation-point heat transfer was used to calculate the parashield stagnation-point heating load at several times during the re-entry trajectory. Thermodynamic properties for air were input from the curve fits[9] based on mixing rules and Sutherland's law viscosity, referenced to the freestream static temperature within the shock layer.[16] Despite the high velocities, these fits were assumed accurate for the parashield because heating rates are relatively moderate on this vehicle, and so static temperatures near the wall are much lower than those typically associated with re-entry surfaces (less than even oxygen dissociation temperatures). The parashield was assumed to have a fully catalytic wall with maximum temperature of 1250 K, beyond which Nextel 312 fails rapidly and catastrophically.

The stagnation-point heat transfer rate vs time and the total heat load to the main shield surface vs time along the re-entry trajectory are presented in Fig. 8. Maximum heat transfer rate is 1.6×10^6 W/m^2 and occurs at 80-km altitude, traveling at 7 km/s. Peak heating occurs 6 min down range, which is relatively early in the trajectory and almost immediately after entering the continuum flow regime. This high early heating is due to the rapid initial deceleration, which in turn is a result of the small ballistic coefficient of the cloth shield. The corresponding total surface energy load is 2.75×10^7 J/m^2.

Main Shield and Spar Heating

The absorption of energy into the parashield surface was modeled as locally one-dimensional heat transfer using a time-forward

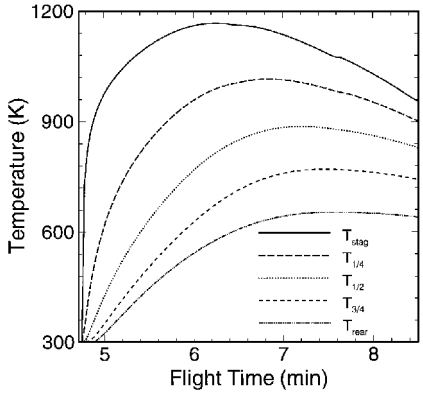

Fig. 9 Parashield LEO re-entry main shield temperature profile history for t_{312} = 6.5 mm and α = 20 deg.

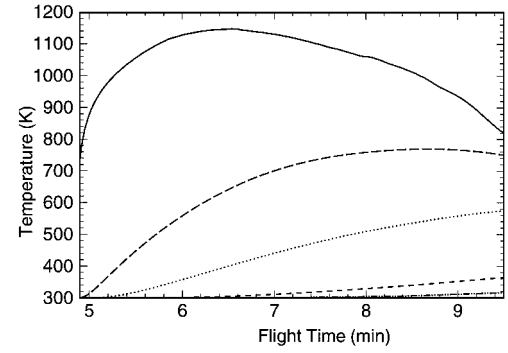

Fig. 10 Parashield LEO re-entry Al 2024 spar temperature profile history for $t_{\text{Al 2024}}$ = 2 mm, t_{312} = 1.65 cm, and α = 20 deg: ——, T_{stag}; – – –, $T_{\text{1/4shield}}$; ·····, $T_{\text{1/2shield}}$; - - - -, T_{spar1}, T_{spar2}; and - ··-, T_{back}.

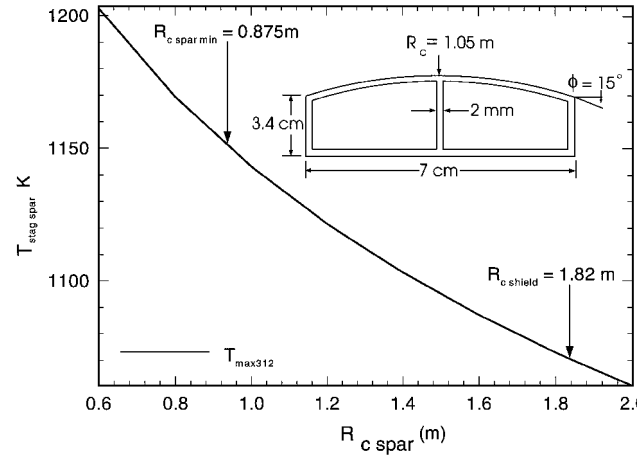

Fig. 11 Parashield LEO re-entry stagnation-point wall temperature vs spar radius of curvature, α = 15 deg.

space-central discretized technique. Nextel 312 is a ceramic-based fabric with a relatively high emmisivity of ≈0.9 (Ref. 14). Therefore, the front and rear shield surfaces were allowed to radiate energy into the boundary layer and the aft flow, but no internal radiation was included. For the analysis of the stagnation-point heating of the parashield spars, only the 2-mm top surface of the beam cross-sectional area was modeled; the actual internal spar structure will likely have low thermal diffusivity, forcing this member to bear the dominant portion of the heat conducted to the spar, such that this simplified model is conservative. It is assumed that a Nextel 312 sleeve would be used to secure the thermal-protection system to the spar, but for the calculation of heat conduction into the freely supported main shield panels, the spar and sleeve sections were not considered.

The flight temperature profiles of the main shield panels were plotted over the parashield trajectory using polynomial curve fits of the thermophysical properties of Nextel 312 (Ref. 14). Cases were run for the 12-paneled parashield baseline geometry over the potential range of re-entry angle of attack. Figure 9 shows the main shield temperature profile history for the parashield at α equal to 20 deg, the worst-case heating profile. To simulate the possible worst-case convection of the shock-layer energy into the wake flow for payload heating,[24] 20% of the stagnation-point heat transfer rate was applied to the payload element over the entire re-entry flight. The payload was assumed to have four layers of Nextel 312, AF-10 for thermal protection, though no wall or shrouding structure was modeled.

The calculated temperature profile demonstrates that a 12-paneled Nextel 312, AF-10 ceramic fiber parashield with the baseline geometry can indeed survive re-entry heating with temperatures below the material limit of 1250 K with a small safety margin at the chosen cloth thickness. Peak surface temperatures are experienced 6 min into the re-entry, corresponding to the peak heating rate. The main shield reaches a maximum surface temperature of 1170 K, and the aft body reaches 750 K. There is, however, a critical heating period lasting about 90 s during which the stagnation-point wall temperature is within 80 K of the Nextel 312 failure limit. These results place further emphasis on the importance of the parashield spar design and the need to accurately predict and avoid severe spar protrusion and associated creation of stagnation-line flow. Note that, as of this writing, newer Nextel materials are in development, such as AF-410, with higher thermal resistivities, lower permeabilities, and similar densities; application of these would obviously increase the thermal margin for the chosen design.[14]

The heating analysis was next modified to account for thermal conduction into the spars themselves. The analysis of stagnation-point heating of the spar-supported shield regions assumed the shield was approximately spherical, as earlier, but with spars that are 2-mm metal dividers between two Nextel 312 regions of varying width. Thermophysical properties of six candidiate spar materials, including titanium, stainless steel, aluminum 2024, beryllium, carbon-carbon composite, and copper, were curve fit vs temperature, for incorporation in a discretized heat absorption model.[1,27] The main shield was found to require a thickness of 6.5 mm, and the attachment sleeve was given the nominal value of 1 mm on each side of the spar. Each spar material's temperature profile was then calculated over the parashield trajectory.

Conductive spars will act as heat sinks throughout the re-entry, lowering the maximum wall temperature by from 20 K (for carbon-carbon) to 60 K (for aluminum); projected maximum internal temperatures in the spars would range between 350 K for aluminum and 800 K for beryllium. Figure 10 shows the temperature history of an aluminum spar. The heat sink effect will also create a local increase in the rear surface temperature of up to 150 K, of possible consequence to the payload.

As estimated earlier, 1500 MPa of fabric pretension would be deployed into the shield panels to avoid concavity. However, as a worst-case scenario, it was of interest to determine a parashield's ability to withstand the heating associated with the most severe fabric concavity possible during LEO re-entry. A minimum value for the radius of curvature of the shield side of the spar was identified by modeling the spar as a cylinder protruding into the stagnation-line flow and calculating its maximum wall temperature over the entire parashield trajectory. Figure 11 shows a plot of the spar radius of curvature vs the maximum generated stagnation-point wall temperature. The minimum local radius of curvature would be 0.875 m; at this value the Nextel 312 shield would reach 1150 K along the spar support, only 100 K below the material thermal limit. Note though that the protruding spar will actually blend smoothly into the shield fabric with the 15-deg tangent angle determined above for the maximum 7% panel concavity, such that an ≈1-m radius-of-curvature spar would survive the stagnation-line thermodynamic loading without simultaneously creating a sharp expansion edge or additional local surface discontinuity in the cloth.

Multiple curves were fitted over varying spar widths to determine the most desirable spar cross-sectional shape.[28] The final width was limited to 7 cm, based on the constraints of the overall vehicle weight

and the central spar attachment plate's dimensions in the baseline vehicle. This results in a 1.05-m stagnation-line radius of curvature through an elliptical surface curve whose tangents are equal to 15 deg at ±3.5 cm. In reality, the shield surface will be further smoothed by its own 6.5-mm thick fabric and the additional spar sleeve. Overall, it was concluded that the radial spars will not create distinct flow protrusions, even in the worst-case panel deformation, for the 12-paneled parashield. The radial spar cross section is shown in Fig. 11.

Although titanium was chosen for the spars on the original parashield design, subsequent heating analysis (see Fig. 10) demonstrates that even Al 2024 spars would survive re-entry if each were wrapped in a 40-layer (1-cm) Nextel 312 protective sleeve. These sleeves on aluminum spars would add 32.5 kg of mass to the baseline shield material. Support of the 34.5-kg shield fabric at the baseline dimensions would require a minimum spar mass of 11 kg with beryllium, compared to titanium at 32 kg, stainless steel at 56 kg, and copper at 63 kg. Carbon-carbon spars would have mass of only 14 kg but would be unlikely to survive re-entry heating even with a Nextel sleeve. Aluminum spars would be 20 kg, but the required Nextel sleeve would make the total spar system mass 53 kg, reducing payload mass by 17 kg compared to the titanium vehicle and by 38 kg for the beryllium spars.

Conclusions

Some of the technical challenges associated with the development of the parashield concept have been outlined, and it is suggested that it is a viable ultralow ballistic coefficient geometry capable of providing aerothermodynamic re-entry shielding to general scientific or commercial payloads. A parashield made of commercially available high-temperature ceramic fabrics, which is supported by a relatively inexpensive aluminum structure, could indeed survive an orbital re-entry. Although studies were focused on a 1.29-m shield radius, the baseline flight-test geometry analyzed in this study could be scaled up by at least a factor of 10, to a radius of 13 m, without significant structural modification. These results are applicable only to re-entry from LEO or less energetic aeromaneuvers, including data drops from the space station or a crew re-entry vehicle for the station. Because of the relatively small heating margin with exisiting fabrics, additional aerothermodynamic analysis would be required before the concept could be accepted for higher energy re-entries such as lunar return.

The baseline 150-kg, 12-paneled parashield has been shown to withstand the aerothermodynamic stagnation-point loading of LEO re-entry with 20–75 kg of payload mass, which could be arranged with a high degree of volumetric freedom, would experience maximum deceleration less than 4 g at an α equal to 15 deg, and would be insensitive to a ±5-deg error in predicting α. Panel heating, fabric permeability, and aerodynamically induced concavity have all been shown to be manageable re-entry issues for a multilayered Nextel 312 AF-10 thermal blanket main shield. Further, any of six common aerospace materials, including Al 2024, would have sufficient structural and thermal integrity over a nominal LEO re-entry trajectory. The lightest weight structure would result in a 45% vehicle payload mass fraction and might even be scaled up to accommodate a human passenger. Optimization could be performed to strike the best compromise between the number of spars and aerothermodynamic performance: the greater the number of spars, and thus the greater the structural mass, the more nearly spherical the shield will be and the less significant will be heating on the spars.

Remaining issues of concern are the effect of chemistry and viscosity on the concaved flowfield and possible schemes for inverting the shield at the end of the re-entry to use it as a parachute. Pressure-induced panel collapse or surface concavity has been identified as a potential source of critical vehicle instability, surface flow complications, and aerothermodynamic failure. A comprehensive review of the full stability derivatives, acoustics, vibrations, and aeroelastics of the parashield has been beyond the focus of this present work. These factors should be a priority in future parashield research and development.

Finally, it is suggested that the design might be improved if highly conductive metal stringers could be placed between the spars, which would improve the parashield's overall re-entry aerothermodynamic performance by conducting heat away from the spar stagnation points. Interpanel copper or stainless steel cabling would also provide fabric support, which would further reduce the likelihood of edge flutter, resist surface concavity and spar protrusion, and conduct significant energy away from the incident main shield surface, though with added mass. When available, the introduction of more advanced Nextel thermal blankets also stands to improve the parashield's thermodynamic re-entry response.

Acknowledgments

A portion of this work has been supported by NASA Grant NAGW-3715, with Isaiah Blankson as Technical Monitor. Russell Howard of the University of Maryland Space Systems Laboratory is also thanked for much helpful advice and information. Appreciation is also expressed to the 3-M corporation for providing data on Nextel 312.

References

[1]Magazu, H. K., "Aerothermodynamic Calculations on the ParaShield Re-Entry Vehicle," M.S. Thesis, Dept. of Aerospace Engineering, UM-AERO 95-19, Univ. of Maryland, College Park, MD, Aug. 1995.

[2]Braun, R. D., and Powell, R. W., "Earth Aerobraking Strategies for Manned Return from Mars," *Journal of Spacecraft and Rockets*, Vol. 29, No. 3, 1992, pp. 297–303.

[3]Raju, I. S., and Craft, W. J., "Analysis and Sizing of Mars Aerobrake Structures," *Journal of Spacecraft and Rockets*, Vol. 30, No. 1, 1993, pp. 102–110.

[4]Tauber, M., Chargin, M., and Henline, W., "Aerobrake Design Studies for Manned Mars Missions," *Journal of Spacecraft and Rockets*, Vol. 30, No. 6, 1993, pp. 656–663.

[5]Freeman, D. C., Powell, R., and Braun, R. D., "Manned Mars Aerobrake Vehicle Design Issues," *Space Technology*, Vol. 12, No. 3, 1992, pp. 313–323.

[6]Gnoffo, P. A., Proce, J. M., and Braun, R. D., "Computation of Near-Wake, Aerobrake Flowfields," *Journal of Spacecraft and Rockets*, Vol. 29, No. 2, 1992, pp. 182–189.

[7]Strawa, A. W., Davy, W. C., and Kruse, R., "Measurements in the Wake of Blunt Aerobrakes at 1.8 km/s and 4.9 km/s," *Journal of Spacecraft and Rockets*, Vol. 30, No. 3, 1993, pp. 380, 381.

[8]Akin, D. L., "The ParaShield Re-Entry Vehicle Concept: Basic Theory and Flight Test Development," *Fourth Annual USU/AIAA Conference on Small Satellites*, Utah State Univ., Logan, UT, Aug. 1990.

[9]Tannehill, J. C., and Mugge, P. H., "Improved Curve Fits for the Thermodynamic Properties of Equilibrium Air Suitable for Numerical Computation Using Time-Dependent or Shock-Capturing Methods," NASA CR-2470, Oct. 1974.

[10]Hankey, W. L., *Re-Entry Aerodynamics*, 1st ed., AIAA, Washington, DC, 1988, pp. 29–36.

[11]*U.S. Standard Atmosphere*, National Oceanographic and Atmospheric Administration, Washington, DC, July 1976.

[12]Adler, P. M., *Porous Media*, 1st ed., Butterworth–Heinemann, Stoneham, MA, 1992, p. 68.

[13]Fogal, G. L., "Air Permeability of Open Weave Fabrics," M.S. Thesis, College of Engineering, Univ. of Maryland, College Park, MD, May 1953.

[14]"Properties of Nextel 312 Ceramic Fibers," 3M Ceramic Materials Dept., Product Testing Data Rept., St. Paul, MN, March 1993.

[15]Brown, R. C., *Air Filtration: An Integrated Approach to the Theory and Applications of Fibrous Filters*, 1st ed., Pergamon, New York, 1994, pp. 29, 30.

[16]Hansen, C. F., "Approximations for the Thermodynamic and Transport Properties of High Temperature Air," NASA TR-R-50, July 1959.

[17]Timoshenko, S., and Woinowski-Kreiger, S., *Theory of Plates and Shells*, 2nd ed., McGraw–Hill, New York, 1959, pp. 313–318.

[18]McGrory, W. D., Slack, D. C., Appelbaum, M. P., and Walters, R. W., "The General Aerodynamic Simulation Program V 2.2," AeroSoft, Inc., Blacksburg, VA, 1993.

[19]Steinbrenner, J. P., Chawner, J. R., and Fouts, C. L., "The GridGen 3-D Multiple Block Grid Generation System," U.S. Air Force Research and Development Center, WRDL-TR-90-3022, Vols. 1 and 2, Wright–Patterson AFB, OH, 1990.

[20]Byars, E. F., Snyder, R. D., and Plants, H. L., *Engineering Mechanics of Deformable Bodies*, 4th ed., Harper and Row, New York, 1983, pp. 309–314.

[21]Strawa, A. W., and Park, C., "Proposed Radiometric Measurement of the Wake of a Blunt Aerobrake," *Journal of Spacecraft and Rockets*, Vol. 29, No. 6, 1992, pp. 765–772.

[22]Engel, C., and Hair, L. M., "Wake Flowfields for a Jovian Probe," NASA CR-159235, March 1980.

[23]Wells, W. L., "Measured and Predicted Aerodynamic Heating on a Cylinder in the Wake of the AFE Configuration at Incidence," AIAA Paper 89-2162, July 1989.

[24]Shieh, P. K., and Gay, A., "Low L/D Aerobrake Heat Transfer Test at Mach 10," *Thermal Design of Aeroassisted Orbital Vehicles*, edited by H. F. Nelson, Vol. 96, Progress in Aeronautics and Astronautics, AIAA, New York, 1985, pp. 378–394.

[25]Dogra, V. K., "Near-Wake Structure for a Generic Configuration of Aeroassisted Space Transfer Vehicles," *Journal of Spacecraft and Rockets*, Vol. 31, No. 6, 1994, pp. 953–959.

[26]Fay, J. A., and Riddell, F. R., "Theory of Stagnation Point Heat Transfer in Dissociated Air," *Journal of the Aeronautical Sciences*, Vol. 25, No. 2, 1958, pp. 73–85, 121.

[27]Incopera, F. P., and DeWitt, D. P., *Fundamentals of Heat and Mass Transfer*, 1st ed., Wiley, New York, 1981, pp. 66–71.

[28]Mason, W. H., and Lee, J., "Aerodynamically Bunt and Sharp Bodies," *Journal of Spacecraft and Rockets*, Vol. 31, No. 3, 1994, pp. 378–382.

B. A. Bhutta
Associate Editor